Microchimica Acta (2024) 191:185
https://doi.org/10.1007/s00604-024-06268-6

ORIGINAL PAPER

Smartphone-assisted hydrogel platform based on BSA-CeO$_2$ nanoclusters for dual-mode determination of acetylcholinesterase and organophosphorus pesticides

Yin Dai[1] · **Wei Xu**[2] · **Xinyi Wen**[1] · **Huizhu Fan**[1] · **Qing Zhang**[1] · **Jun Zhang**[1] · **Hongsong Zhang**[3] · **Wanying Zhu**[1] · **Junli Hong**[1]

Received: 8 December 2023 / Accepted: 17 February 2024 / Published online: 7 March 2024

Abstract

A dual-mode sensor was developed for detecting acetylcholinesterase (AChE) and organophosphorus pesticides (OPs) via bifunctional BSA-CeO$_2$ nanoclusters (NCs) with oxidase-mimetic activity and fluorescence property. The dual-mode sensor has the characteristics of self-calibration and self-verification, meeting the needs of different detection conditions and provide more accurate results. The colorimetric sensor and fluorescence sensor have been successfully used for detecting AChE with limit of detection (LOD) of 0.081 mU/mL and 0.056 mU/mL, respectively, while the LOD for OPs were 0.9 ng/mL and 0.78 ng/mL, respectively. The recovery of AChE was 93.9–107.2% and of OPs was 95.8–105.0% in actual samples. A novel strategy was developed to monitor pesticide residues and detect AChE level, which will motivate future work to explore the potential applications of multifunctional nanozymes.

Keywords Acetylcholinesterase · Organophosphorus Pesticides · Dual-mode sensor · Oxidase-mimetic activity · Hydrogel platform · Smartphone color detection

Introduction

An important role played by AChE, which could hydrolyze acetylthiocholine (ATCh) into thiocholine (TCh), was keeping ATCh levels in check [1]. Studies have shown that imbalances of ATCh can lead to numerous neurodegenerative diseases, like Alzheimer's dementia, Parkinson's disease and myasthenia gravis [2–4]. Hence, it was extremely important to monitor AChE levels and screen for potential inhibitors. The misuse of organophosphorus pesticides (OPs) in recent years has posed major ecological and human health problems [5]. Furthermore, the OPs inhibited irreversibly the AChE and caused abnormal accumulation of ATCh, resulting in various diseases and ultimately death [6]. Most of the current methods for detecting pesticide residues required expensive instrument and complicated operation such as high performance liquid chromatography with photo-diode array detector, surface-enhanced Raman spectroscopy and electrochemical methods (e.g. square wave voltammetry, differential pulse voltammetry, etc.), making it impossible for rapid and real-time detection [7–9]. Thus, it is imperative to design a reliable onsite detection way for OPs residues in food and environment.

Nanozymes have attracted more attention in recent years due to the high stability, modifiable catalytic activity and low cost [10]. However, most of the current nanozyme-based sensors were limited to single-mode detection, existing disadvantages such as false positives or false negatives [11]. The dual-mode sensor not only possessed inherent self-calibration and self-verification capabilities, but can also met the requirements of different detection conditions, promising more reliable detection results [12, 13]. Nanoclusters, as common fluorescence material, exhibited enzyme-like catalytic activity, making them a potential bifunctional nanozymes [14, 15]. However, few studies have combined the enzyme-like catalytic properties of NCs with their

✉ Junli Hong
junlihong@njmu.edu.cn

[1] School of Pharmacy, Nanjing Medical University, Nanjing 211166, Jiangsu, China

[2] Jiangsu Provincial Hospital of Chinese Medicine, Nanjing 210004, Jiangsu, China

[3] Department of Cardiology, Nanjing First Hospital, Nanjing Medical University, Nanjing 210006, Jiangsu, China

fluorescence properties to achieve multimodal sensing of analytes [16]. Therefore, our group have synthesized BSA-CeO_2 NCs by doping bovine serum albumin (BSA), which with great fluorescence properties and the oxidase-like property, meeting the demands of fluorescence and ultraviolet (UV) detection. Although this method could be influenced by the instability of natural enzymes, it still could provide more accurate detection results. Therefore, the bifunctional nanozyme can provide a promising approach for dual-mode analysis.

Sodium alginate was able to crosslink with divalent cations (e.g. Ca^{2+}, Zn^{2+} and Co^{2+}) to form a hydrogel in aqueous solution, which was a green and gentle way [17]. The hydrogel matrix provided a relatively inert environment and allowed molecules to diffuse through the porous structure, enhancing the stability and functionalization of the material [18, 19]. Importantly, the hydrogel platform demonstrated a more distinct catalytic signal in function of the same condition than that of the aqueous solution, owing to the highly hydrophilic environment [20, 21]. Meanwhile, the constructed hydrogel platform could aggregate oxidation product, bringing about more significant color change [22]. These colors can be converted to specific RGB values by an application called "Color Detector" on a smartphone, realizing the real-time monitoring of the analyte on site [23]. The ability to analyze data rapidly of smartphone combined with the portability of hydrogels, exhibiting the potential to serve as a cost-effective and user-friendly point-of-care sensor [24, 25].

A novel bifunctional BSA-CeO_2 NCs was prepared for the dual-mode ratiometric fluorescence/colorimetric quantification of AChE and OPs. The nanoclusters were modified by doping BSA, which could keep a steady microenvironment and prevent the CeO_2 NCs from being reduced. The BSA-CeO_2 NCs with enzyme-like catalytic ability enable to catalyze colorless o-phenylenediamine (OPD) to yellow 2,3-diaminophenothiazine (DAP) for colorimetric detection. In the presence of AChE, the UV signal was weakened attributing to the production of reductive TCh, which could be recovered with OPs or AChE inhibitors. On the other side, the fluorescence of BSA-CeO_2 NCs at 440 nm was decreased by DAP (550 nm) because of fluorescence resonance energy transfer (FRET), enabling ratiometric fluorescence detection. In the pathway for detecting AChE, the fluorescence signal of the BSA-CeO_2 NCs recovered as the DAP decreased (fluorescence at 570 nm weakened). However, the presence of OPs or AChE inhibitors inhibited the AChE and correspondingly increased DAP generation, resulting in the fluorescence of BSA-CeO_2 NCs reduced. This study not only realized the dual-mode detection of dual targets, but also applied to the real-time monitoring of pesticides with the help of hydrogel platform and smartphone (Scheme 1C). In brief, this study offered a promising strategy for the dual-mode quantification of analytes, simultaneously inspiring the application of nanozyme in point-of-care detection.

Experimental section

Reagents and apparatus

All reagents and apparatus were provided in the Supplementary material.

Synthesis of BSA-CeO_2 NCs

The BSA-CeO_2 NCs were synthesized by a BSA incubation strategy according to the previous method [26]. Typically, 125 mg BSA powders were dissolved in 50 mL deionized water at 37 °C along with magnetic stirring, and 1 mL $(CH_3COO)_3Ce\cdot xH_2O$ solution (42 mg/mL) was gradually added. Then, NaOH was added to the solution to adjust its pH to 10–11. After 6 h reaction, BSA-CeO_2 NCs powder was obtained via freeze drying.

The oxidase-like activity of BSA-CeO_2 NCs

The OPD was utilized as catalytic substrate to study the oxidase-like activity of BSA-CeO_2 NCs. The first step was to mix 50 μL BSA-CeO_2 NCs (20 μg/mL) and 50 μL OPD (10 mM) with 200 μL acetic acid-sodium acetate buffer solution (ABS) (pH 4.0, 0.2 M). The UV absorption spectrum was obtained after reacting for 0.5 h.

In order to determine the kinetic constants, we assayed the absorbance at 650 nm for different concentrations of TMB systems. 50 μL BSA-CeO_2 NCs were mixed with 100 μL of ABS and 50 μL of different concentrations of TMB. The Km of BSA-CeO_2 NCs was calculated as follows [27]:

$$V_0 = V_{max} \times \frac{[S]}{k_m + [S]} \tag{1}$$

Fluorescence property of BSA-CeO_2 NCs

The fluorescence signal of BSA-CeO_2 NCs was investigated following: 50 μL BSA-CeO_2 NCs was added to 250 μL ABS. The fluorescence curve was recorded under 380 nm as the excitation wavelength. The collection of fluorescence spectra in the emission ranged from 400 to 650 nm.

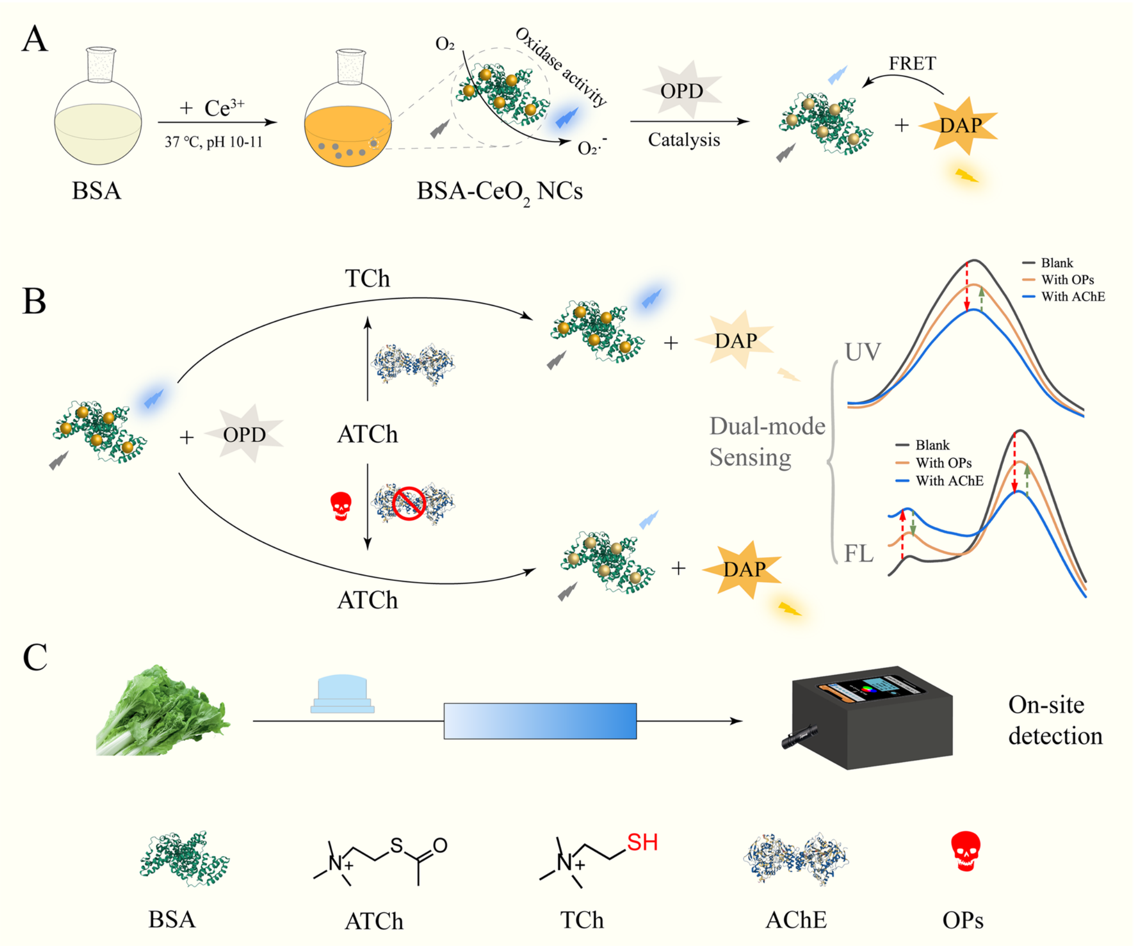

Scheme 1 **A** Illustration of the synthesis of BSA-CeO$_2$ NCs. **B** Dual-mode determination of AChE and OPs. **C** On-site detection of OPs residue in vegetables based on smartphone-assisted hydrogel platform

Dual-mode determination of AChE and OPs

Different concentrations of AChE and 20 μL ATCh (10 mM) were dispersed to Tris–HCl buffer solution (pH 7.4, 50 mM), and the total system was mixed evenly with 300 μL and incubated at 37 °C for 0.5 h. Then, 50 μL of the above system was reacted with 50 μL BSA-CeO$_2$ NCs, 50 μL OPD and 150 μL ABS. Following reaction for 0.5 h, the fluorescence and the UV spectra were obtained.

The potential impacts of OPs were also assessed on the BSA-CeO$_2$ NCs + AChE + ATCh system. In the first step, the concentration of AChE was fixed (final concentration was 25 mU/mL), and different concentrations of CPF were added for subsequent experiments. The subsequent experimental procedure was the same as AChE determination.

Screening of AChE inhibitors from natural alkaloids

The acetylcholinesterase inhibitory activity of four natural alkaloids (berberine hydrochloride, camptothecin, matrine, and evodiamine) was investigated using donepezil as a positive control. Firstly, 12 μL alkaloids (10 mM), 30 μL AChE (1 U/mL) and 20 μL ATCh (10 mM) were dispersed to Tris–HCl buffer solution. The following steps were the same as detecting CPF, and the absorbance values were acquired at 450 nm (A$_1$). Parallel experiments were also carried out without the alkaloids (A) and without the alkaloids and AChE (A$_0$). The calculation of inhibition rate [28] was performed using formulas (2).

$$Inhibition\ (\%) = \frac{A_1 - A}{A_0 - A} \times 100 \tag{2}$$

On-site detection of OPs via hydrogel sensor

Sodium alginate (10.0 mg) was added to the BSA-CeO$_2$ NCs (50 μL) + TMB (10 mM, 50 μL) + ABS (150 μL) system and incubated for 10 min. The 10 μL CaCl$_2$ solution (60 mM) and 10 μL poly(acrylic acid) (PAA) (5 mM) were dropped into obtained viscous liquid and inverted the centrifugal tube to obtain hydrogel spheres in the snap cap of centrifugal tube. Meanwhile, different concentrations CPF were reacted with AChE (1 U/mL, 60 μL) and ATCh (10 mM, 20 μL) in Tris–HCl buffer solution at 37 °C for 0.5 h. Subsequently, 50 μL reaction solution was dropped into the hydrogel sensor at room temperature for 10 min and recorded the RGB value by the color recognition application on a smartphone.

Analysis of AChE and OPs in actual samples

In order to investigate the practicality of this method, actual samples were analyzed [29]. The protein precipitate was obtained by mixing the whole blood sample with 10% trichloroacetic acid (v/v, 1:1) and ice bath for 10 min. Above mixture was centrifuged at 12,000 rpm for 15 min to obtain the supernatant of the suspension, which was used for the subsequent AChE assay. Specifically, 20 μL supernatant was reacted with ATCh (10 mM, 20 μL) in Tris–HCl buffer solution for 0.5 h firstly. Then 50 μL reaction solution was incubated with 50 μL BSA-CeO2 NCs, 50 μL OPD and 150 μL ABS for 0.5 h for further quantification.

The actual samples used for determination of CPF residue were river water and apples, collecting from the local supermarket and Tianyuan river. Firstly, 2.0 g of apples was added to 10 mL of ethanol and extracted by ultrasonication for 2 h. The extracted food samples and water samples were then centrifuged at 12,000 rpm for 10 min and the supernatant was collected for further analysis [30]. Subsequently, colorimetric and fluorescence measurements were carried out using the same methods as in section of “Dual-mode determination of AChE and OPs”.

Results and discussion

Feasibility and sensing strategy

The synthesis of BSA-CeO_2 NCs was depicted in Fig. 1A. The prepared BSA-CeO_2 NCs exhibited great fluorescence property and oxidase-like activity, which could catalyze the

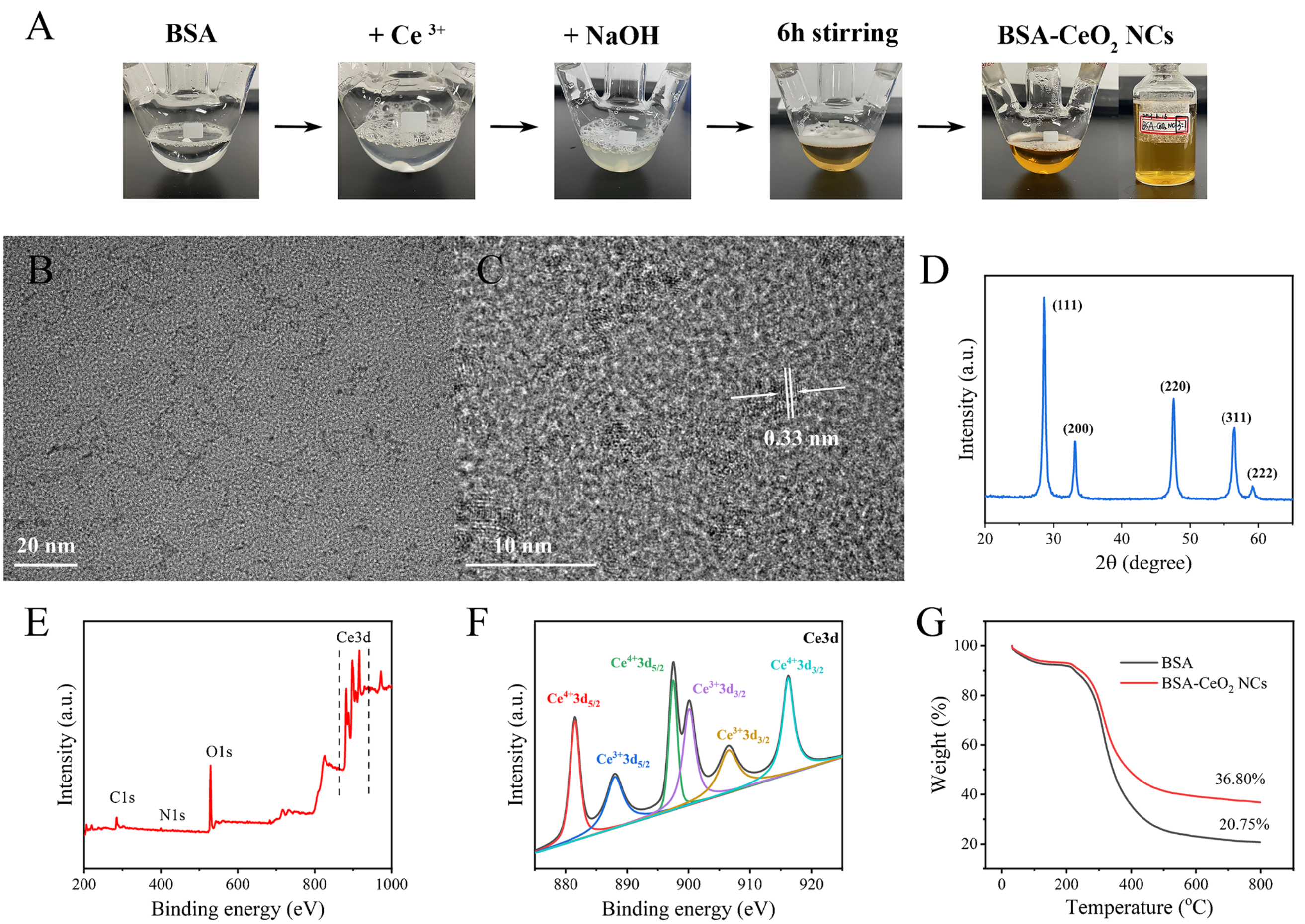

Fig. 1 **A** Synthesis process of BSA-CeO_2 NCs. **B**–**C** HRTEM images of BSA-CeO_2 NCs. **D** XRD pattern of BSA-CeO_2 NCs. **E** XPS results of BSA-CeO_2 NCs. **F** Ce3d spectra of BSA-CeO_2 NCs. **G** TGA analysis of BSA-CeO_2 NCs and BSA

production of $O_2^{\cdot -}$ from free oxygen. The generated $O_2^{\cdot -}$ can oxidize the colorless OPD to the yellow oxidation state DAP, exhibiting the UV signal. Moreover, a FRET effect between the DAP and BSA-CeO_2 NCs occurred, resulting in decreased fluorescence of BSA-CeO_2 NCs (Scheme 1A).

As displayed in Scheme 1B, ATCh can be catabolized by AChE to produce TCh. And the TCh with sulfhydryl groups (-SH) inhibited the oxidase-mimetic properties of the BSA-CeO_2 NCs, leading to a reduction in DAP content and thus a weakening of the UV signal. Meantime, FRET was also inhibited and the DAP fluorescence signal was reduced while the fluorescence signal of the BSA-CeO_2 NCs was restored. Nevertheless, OPs could inhibit AChE activity, resulting in reduced TCh production and restoration of absorbance. Meanwhile, DAP fluorescence enhanced and NCs fluorescence decreased. As a result, a dual-mode sensor capable of measuring AChE and OPs simultaneously was developed.

Characterization of BSA-CeO_2 NCs

The morphology and lattice structure of BSA-CeO_2 NCs were investigated by high-resolution transmission electron microscopy (HRTEM) (Fig. 1B and 1C). The BSA-CeO_2 NCs were uniformly distributed and approximately 2 nm in diameter. The lattice spacing of 0.33 nm was belonged to (111) plane of CeO_2 that was in accordance with X-ray diffraction (XRD) result [31, 32]. The XRD patterns (Fig. 1D) displayed several diffraction peaks of CeO_2 structure, including the (111), (200), (220), (311) and (222) crystal planes [33]. The X-ray photoelectron spectroscopy (XPS) were explored to reveal the elemental compositions and chemical states of the BSA-CeO_2 NCs. The results of XPS (Fig. 1E) and table of elemental content (Table S1) showed that the nanoclusters contained C, N, O and Ce (Fig. 1F and Fig. S1). In the Ce3d spectrum in Fig. 1E, the peak at 888 eV, 900.1 eV and 906.5 eV were ascribed to Ce^{3+} and other peaks at 881.5 eV, 897.5 eV and 916.2 eV were related to Ce^{4+} in the prepared nanoclusters [34, 35]. The weight ratio of CeO_2 clusters was calculated by thermogravimetry analysis (TGA) and represented 16.05% of the weight of BSA-CeO_2 NCs (Fig. 1G) [36]. The UV–vis spectroscopy of BSA-CeO_2 NCs was depicted in Fig. S2, indicating that the absorption peak of Ce–O bonding was around 330–340 nm and the peak around 280 nm attributed to BSA [37]. Above information confirmed the successful preparation of the BSA-CeO_2 NCs.

Oxidase-like activity of BSA-CeO_2 NCs

As can be seen in Fig. 2A, there was no UV absorption from the OPD and BSA-CeO_2 NCs alone. However, an evident UV absorption at 450 nm occurred when OPD coexisted with BSA-CeO_2 NCs, supporting that OPD was oxidized to DAP. In Fig. 2B, when AChE and ATCh were presented in the system of BSA-CeO_2 NCs and OPD, the UV absorbance was significantly reduced, demonstrating that the generation of TCh with -SH possessed inhibitory effect on the oxidase-like activity of BSA-CeO_2 NCs (curve b). Nevertheless, OPs could inhibit AChE activity, resulting in reduced TCh production and restoration of absorbance (curve c). The Electron spin resonance (ESR) experiments were used to investigate the radicals generated by of BSA-CeO_2 NCs + OPD system. As shown in Fig. 2C, a clear superoxide radical ($O_2^{\cdot -}$) signal was captured, indicating that BSA-CeO_2 NCs possessed oxidase-like activity. Furthermore, the effect on the reaction system of different reactive oxygen species scavengers were studied, including isopropanol (·OH), tryptophan ($^1O_2$), catalase (H_2O_2) and p-benzoquinone ($O_2^{\cdot -}$) as scavenger. The absorbance of the system decreased only in the presence of p-benzoquinone, proving that the existence of $O_2^{\cdot -}$ in the reaction system (Fig. 2D). In addition, BSA-CeO_2 NCs could also effectively catalyze other chromogenic substrates (TMB, ABTS, etc.), demonstrating great substrate universality (Fig. S3).

Additionally, the Km of BSA-CeO_2 NCs was shown in Fig. S4. Meanwhile, the oxidase-like activity of BSA-CeO_2 NCs prepared with diverse ratios of BSA and CeO_2 were compared in Table S2. And the optimal ratio of BSA and CeO_2 was 3: 1.

Fluorescence property of BSA-CeO_2 NCs

The fluorescence property of BSA-CeO_2 NCs was evaluated in detail under the excitation wavelength of 380 nm. As displayed in Fig. 3A, the fluorescence emission of the BSA-CeO_2 NCs was approximately 440 nm. In addition, OPD itself does not fluoresce; When BSA-CeO_2 NCs co-existed with OPD, OPD oxidized to DAP, and fluorescence was generated at 570 nm. FRET between DAP and BSA-CeO_2 NCs led to a reduction in the fluorescence of BSA-CeO_2 NCs, thereby constructing a ratiometric fluorescence sensor. In Fig. 3B, following the successive addition of AChE + ATCh and incubation with BSA-CeO_2 NCs, the fluorescence intensity of the DAP decreased evidently and the fluorescence of BSA-CeO_2 NCs recovered (curve b). The results showed that TCh inhibited oxidase activity, DAP production was reduced, FRET was weakened, and the fluorescence of NC was restored. However, OPs can inhibit AChE activity, resulting in reduced TCh production, resulting in enhanced DAP fluorescence and decreased NC fluorescence (curve c).

The fluorescence quenching mechanism was also investigated. The UV absorption spectrum of DAP overlapped with the fluorescence spectrum of BSA-CeO_2 NCs, suggesting there was a FRET or inner-filter effect (IFE) between the NCs and DAP (Fig. 3C). Meanwhile, fluorescence lifetime

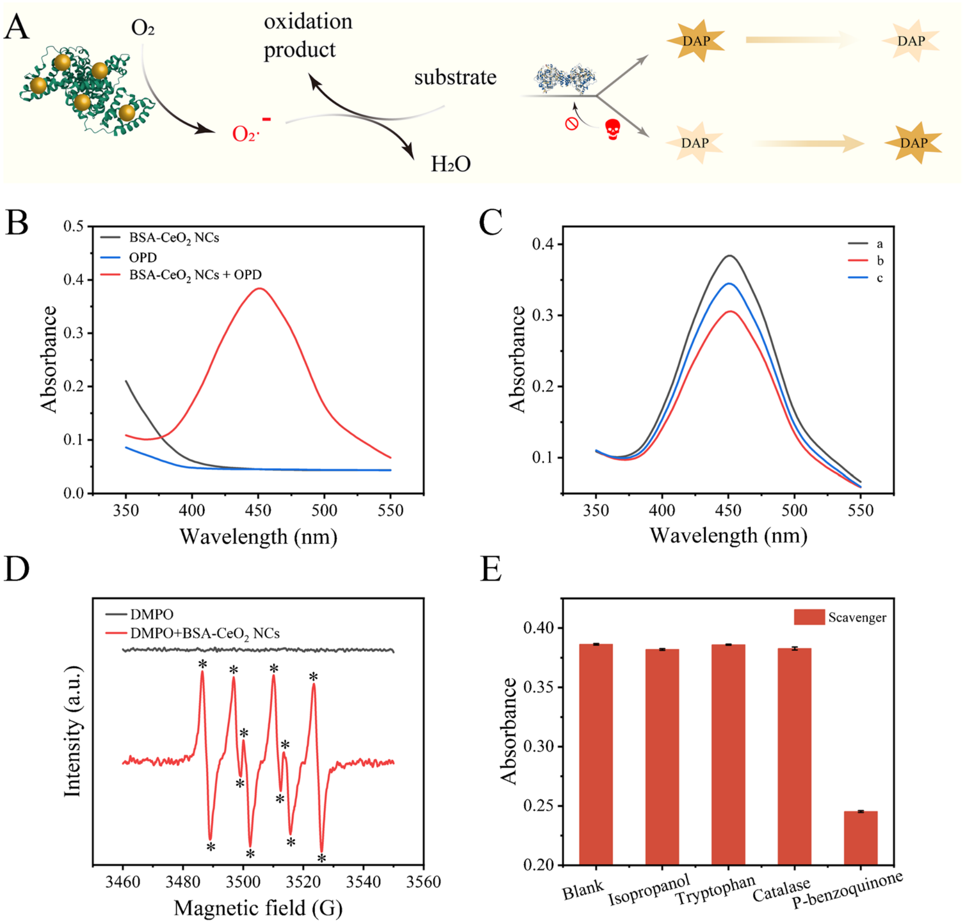

Fig. 2 **A** Oxidase-like mechanism of BSA-CeO$_2$ NCs using in detection. **B** UV curve of various systems. **C** Effects of different target on the catalytic reaction: (a) BSA-CeO$_2$ NCs + OPD, (b) BSA-CeO$_2$ NCs + OPD + AChE + ATCh, (c) BSA-CeO$_2$ NCs + OPD + AChE + ATCh + OPs. (D) ESR spectrum comparison of 5,5-dimethyl-1-pyrroline N-oxide (DMPO) and DMPO + BSA-CeO$_2$ NCs in ethanol. (E) The results of the system under various scavengers

was also investigated to further determine the mechanism (Fig. 3D). Due to the fluorescence lifetime reduction of BSA-CeO$_2$ NCs in the presence of DAP, it was clear that FRET has taken place.

Dual-mode determination of AChE and OPs

To ensure the dual-mode sensor was carried out under ideal conditions, related factors were optimized. In colorimetric detection mode, the incubation time of AChE + ATCh was 0.5 h (Fig. S5A) and the BSA-CeO$_2$ NCs + AChE + ATCh + OPD system was incubated at pH = 4 and 37 °C for 30 min (Fig. S5B-D). Additionally, the ratiometric fluorescence detection was under the same condition (Fig. S6).

In Fig. S7A-B, the absorbance at 450 nm of the BSA-CeO$_2$ NCs + AChE + ATCh + OPD system was reduced because of AChE. The linear range was 0.1–25 mU/mL ($Y = -0.0026X + 0.372$, $R^2 = 0.998$), while the LOD was 0.081 mU/mL based on the 3δ/slope. On the other hand, the fluorescence value of the BSA-CeO$_2$ NCs (F_{570}) moderately increased and the intensity of DAP (F_{440}) weakened with the increasing concentration of AChE (Fig. S7C-D). The linear equation was Y (F_{440}/ F_{570}) = 0.0115X + 0.526 (0.1–25 mU/mL, $R^2 = 0.994$), while the LOD was 0.056 mU/mL. Compared with other methods, the dual-mode sensor designed has higher sensitivity and wider linear range (Table S3).

As depicted in Fig. 4A-C, the UV absorbance of the BSA-CeO$_2$ NCs + AChE + ATCh + OPs + OPD system (CPF chosen as a representative OPs) was linearly with the logarithm of CPF concentration (ln[CPF]) ranging from 0.001 to 6 μg/mL ($Y = 0.007\ln X + 0.347$, $R^2 = 0.995$). Moreover, the LOD was as low as 0.9 ng/mL. On the other hand, the fluorescence ratio (F_{570}/F_{440}) was linearly with the ln[CPF] (Fig. 4D-F). The linear equation was Y (F_{570}/ F_{440}) = 0.0863lnX + 1.834 ($R^2 = 0.992$, 0.001–6 μg/mL), while the LOD was 0.78 ng/mL. Overall, these results suggested that the dual-mode sensor outperformed other OPs detection strategies (Table S4).

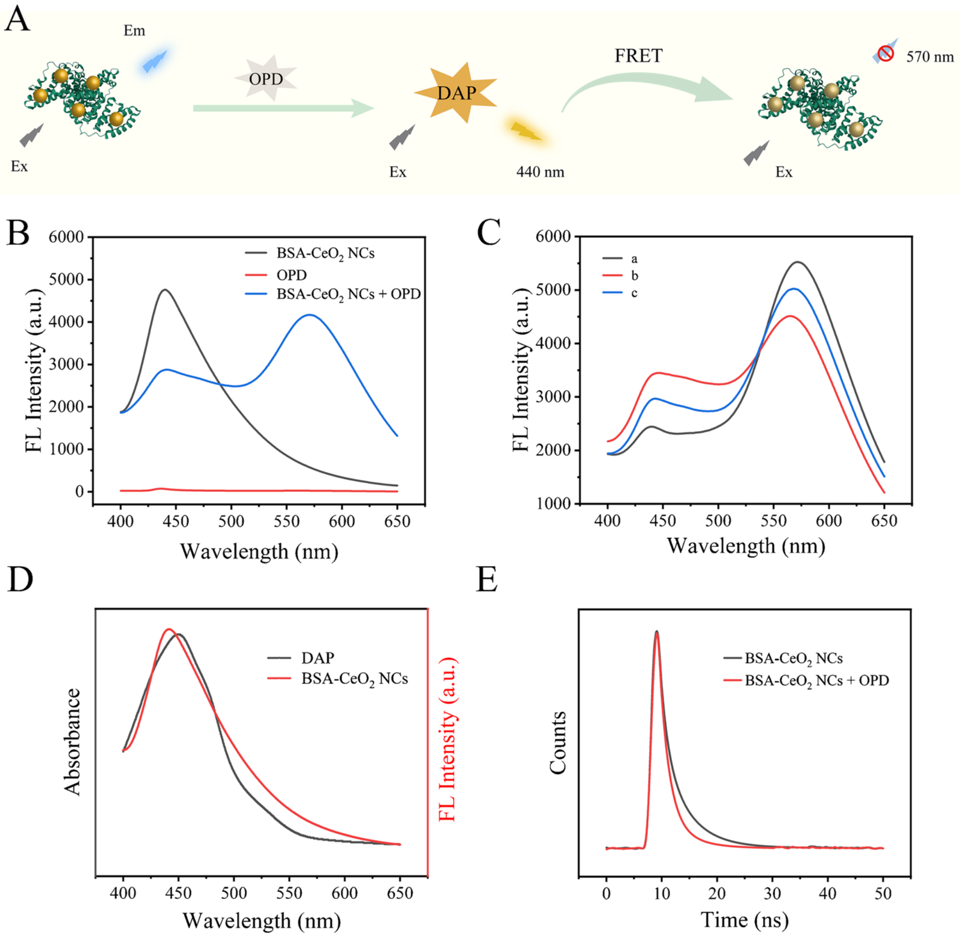

Fig. 3 **A** Fluorescence detection mechanism based on FRET effect. **B** Fluorescence spectra of different system. **C** Effects of diverse analyte on fluorescence of NCs: (a) BSA-CeO$_2$ NCs + OPD, (b) BSA-CeO$_2$ NCs + OPD + AChE + ATCh, (c) BSA-CeO$_2$ NCs + OPD + AChE + ATCh + OPs. **D** UV spectrum of DAP and fluorescence spectrum of BSA-CeO$_2$ NCs. **E** Fluorescence lifetime results of NCs with and without OPD

Screening of natural AChE inhibitors

The effects of four alkaloids on AChE were evaluated at a concentration of 100 μM. The inhibition result in the presence of various alkaloids was shown in Fig. 5C. It was clear that berberine hydrochloride exhibited an outstanding inhibition effect on AChE. Additionally, the inhibition rate of donepezil (used for the treatment of Alzheimer's disease) was calculated as 91.98% and the inhibition rate of berberine hydrochloride was 88.34% (Table S5). These results suggested that the method could be used to screen for AChE inhibitors from natural alkaloid, which was of great importance for the early diagnosis and treatment of nervous system diseases.

Study of selectivity and stability

Further investigation was conducted into the selectivity, anti-interference ability, and stability of the sensor. In Fig. 5A, only AChE could induce an obvious change in the sensing signal of the BSA-CeO$_2$ NCs + ATCh + OPD system. Additionally, the sensor's response did not change when interferents and AChE were added to the system (Fig. 5B), indicating distinguished anti-interference capability.

In the system for determination OPs, only OPs (such as CPF, ETH, DDVP and ACEP) (Fig. S8) significantly affected the response of the dual-mode sensor, while other non-OPs and interfering ions had no significant effect (Fig. 5D). The impact of OPs on the sensor was further explored via statistical analysis. Since principal component analysis (PCA) could recognize linear combinations of features that differentiate among more events types, it maximizes the variance ratio of events and results in maximum data separation [38]. In Fig. 5E, the results of OPs were classified into four categories, demonstrating that CPF can be easily distinguished from other OPs using the sensing strategy we developed.

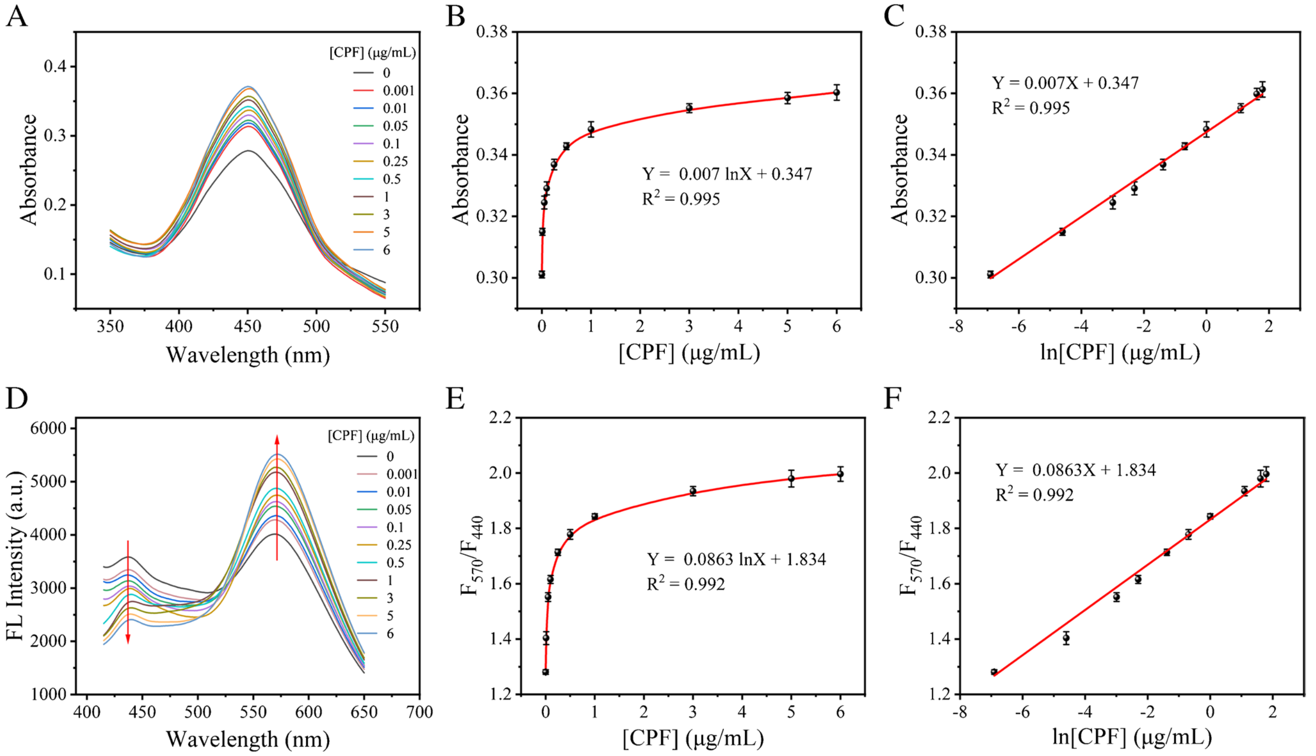

Fig. 4 **A** UV absorption spectra of the BSA-CeO_2 NCs + AChE + ATCh + OPs + OPD system with different levels of CPF. **B** The UV signal value varied with CPF. **C** The linear relationship between the absorbance and ln[CPF]. **D** The fluorescence responses of the system with diverse content of CPF. **E** The F_{570}/F_{440} varied with CPF. **F** The linear relationship between the F_{570}/F_{440} and ln[CPF]

Furthermore, the fluorescence and colorimetric response could remain almost constant, although BSA-CeO_2 NCs had been kept at 4 °C for 3 months (Fig. 5F).

On-site determination of OPs based on hydrogel platform

The dual-mode sensor could be further applied for on-site detection of OPs based on smartphone and hydrogel platform. As displayed in Fig. 6A, the hydrogel platform was developed using TMB as chromogenic substrate to obtain noticeable color changes. The color information of photographs was gathered from a color recognition application called "Color Detector" on the smartphone (as shown in Fig. S9). In order to exclude the interference of external light sources on the results, we also designed a smartphone-assisted sensing platform, including a dark box, a fixed light source and a fixed smartphone (Fig. S10). The values of B/R were linearly related ($Y = 0.2192X + 1.6457$, $R^2 = 0.996$) to CPF content from 0.1 to 40 μg/mL (Fig. 6D), while the LOD was 49.5 ng/mL. Compared with the linear relationship in solution (Fig. 6C), hydrogel platform exhibited more obvious color change under the same condition, owing to the highly hydrophilic environment of the hydrogel layer. Accordingly, the proposed sensor allowed on-site visual detection of OPs residues.

Determination of AChE in human serum

To investigate the reliability and practicability of the sensor, determination of AChE in human serum was carried out. The samples were also tested for recovery by adding different concentrations of AChE (80%, 100% and 120% of detected concentrations) to the samples. The recoveries of ratiometric fluorescence detection modes were calculated ranging from 97.5% to 107.2% and the results of the colorimetric mode ranged from 93.9% to 105.6% (Table S6), exhibiting excellent reliability for AChE determination in real samples.

Quantification of CPF in actual samples

The dual-mode sensor was used for the quantification of CPF utilizing vegetables and river water as the real samples. Different concentrations of CPF were added to the pretreated samples to determine the recovery rate. With the dual-mode analysis (Table 1), the recoveries were 95.8–105.0% (colorimetric mode) and 95.8–104.0% (ratiometric fluorescence

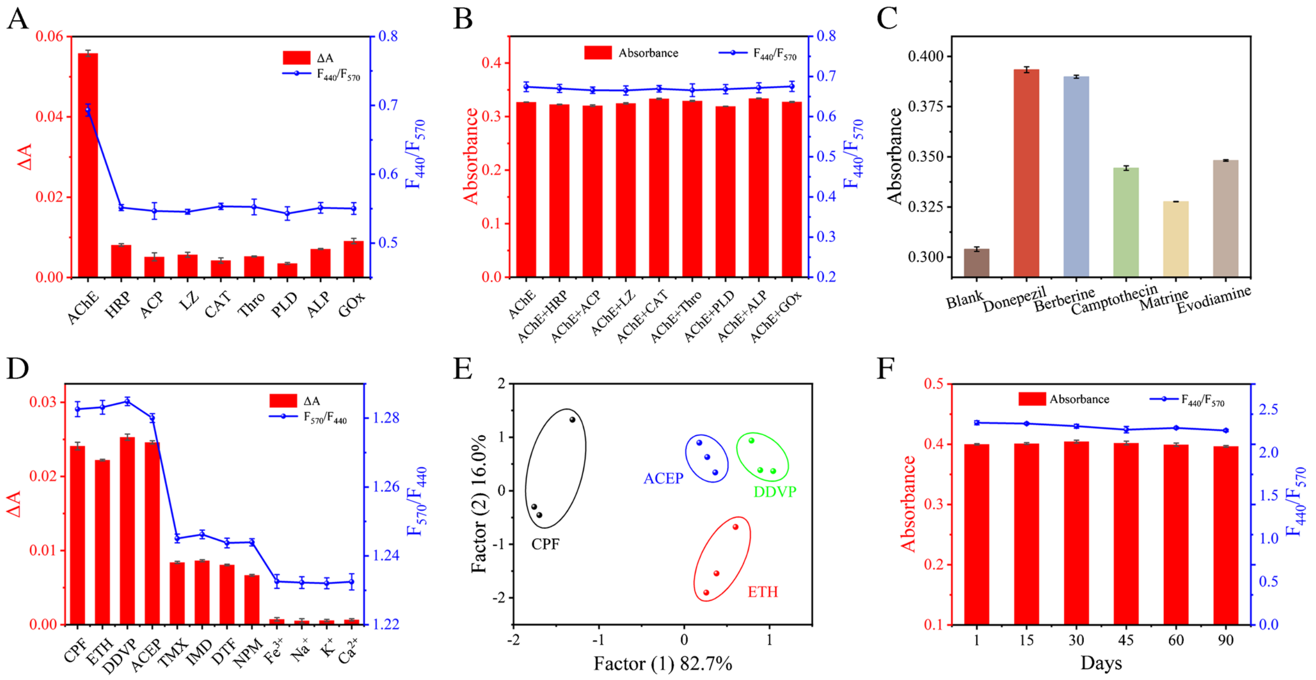

Fig. 5 **A** The selectivity and (**B**) anti-interference ability of the system for AChE determination (10 mU/mL) with diverse interferents (100 mU/mL). Interferents included horseradish peroxidase (HRP), acid phosphatase (ACP), lysozyme (LZ), catalase (CAT), thrombin (Thro), phospholipase D (PLD), alkaline phosphatase (ALP) and Glucose oxidoreductase (GOx). **C** Absorbance values at 450 nm of the BSA-CeO_2 NCs + OPD + ATCh + AChE + various alkaloids system. **D** The selectivity of the system for OPs determination (0.1 μg/mL) with the interfering substance (1 μg/mL). interferents included ethoprophos (ETH), dichlorovos (DDVP), acephate (ACEP), thiamethoxam (TMX), imidacloprid (IMD), dinotefuran (DTF), Nitenpyram (NPM), Fe^{3+}, Na^+, K^+ and Ca^{2+}. **E** Canonical score plots for the detection response to CPF, ACEP, DDVP and ETH were analyzed by PCA. **F** The stability of BSA-CeO_2 NCs over time

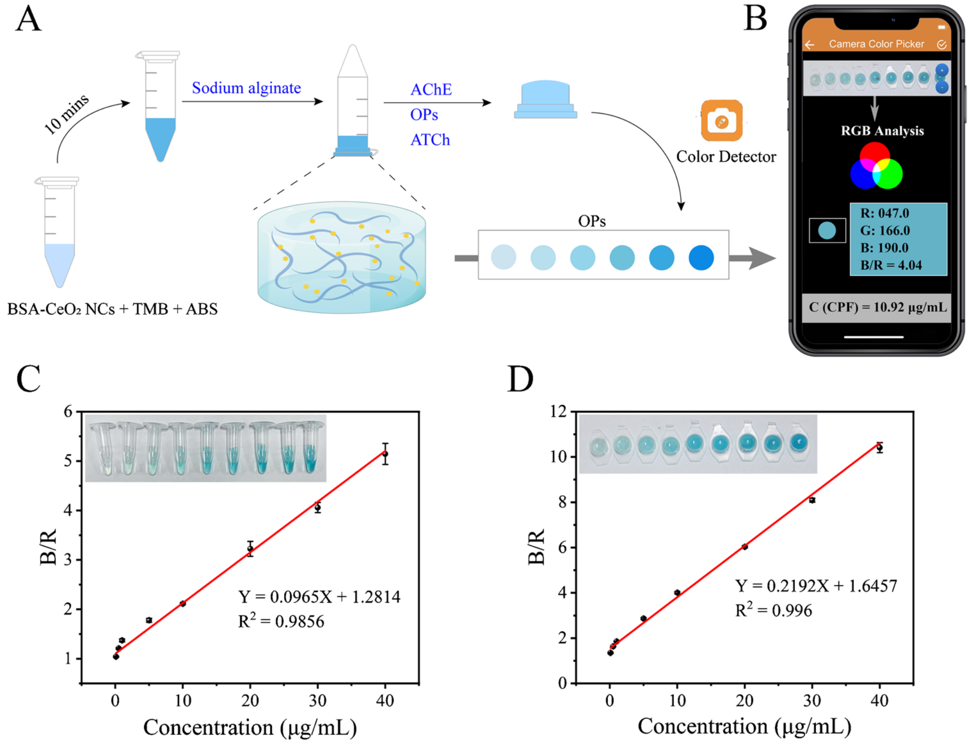

R: 047.0
G: 166.0
B: 190.0
B/R = 4.04

C (CPF) = 10.92 μg/mL

Fig. 6 **A** Illustration of the preparation and the sensing principle of hydrogel platform. **B** RGB information of photos was collected from a color recognizer application. **C** Linear relationship of the values of B/R versus CPF concentration in solution and **D** in hydrogel. Inset: corresponding color images

Table 1 Determination results of CPF in real samples (*n* = 3)

Sample	Detected (μg/mL)	Added (μg/mL)	Colorimetric sensor			Fluorescence sensor		
			Found (μg/mL)	Recovery (%)	RSD (%)	Found (μg/mL)	Recovery (%)	RSD (%)
Vegetables	ND	0.100	0.105	105.0	0.49	0.102	102.0	0.43
		1.00	0.991	99.1	0.24	0.975	97.5	0.41
		5.00	4.93	98.6	0.19	4.79	95.8	0.24
Tianyuan lake		0.100	0.101	101.0	0.23	0.099	99.0	0.89
		1.00	0.972	97.2	0.10	1.03	103.0	0.72
		5.00	4.79	95.8	0.43	5.20	104.0	0.38

ND = not detected (or < LOD)

mode). The results indicated that the sensor exhibited outstanding practical application prospects for CPF detection. Furthermore, the colorimetric analysis was in accordance with the ratiometric fluorescence results, indicating that the quantification results were validated mutually.

Conclusion

In this study, a dual-mode sensor based on BSA-CeO_2 NCs with oxidase-mimetic activity and optical property has been designed for the determination of AChE and OPs, which also offered a new way for screening of AChE inhibitors from natural alkaloid. Since the catalytic activity of BSA-CeO_2 NCs could be inhibited by TCh, the hydrolysate of AChE, leading to the oxidase-like activity decreased, AChE could be detected based on this principle. And the inactivation behavior of OPs toward AChE allowed for detecting OPs. Meanwhile, we further established a hydrogel platform with smartphone-assisted for on-site detection. Although the accuracy needed to be improved compared with dual-mode detection, it can meet the demand of on-site, portable, and rapid analysis of OPs residue in food and environment. This study not only enabled the use of nanozymes in pesticide detection, but also provided inspiration for the use of nanozymes in the screening of natural AChE inhibitors.

Supplementary Information The online version contains supplementary material available at https://doi.org/10.1007/s00604-024-06268-6.

Funding This work was supported by the National Key R&D Program of China (No. 2022YFA1104800 and 2021YFF1200800), Medical Research Foundation of Jiangsu Commission of Health (No. Z2020009), National Natural Science Foundation of China (No. 22274079, 21904069, 81202853, 82200497), the Foundation of Anhui Province Key Laboratory of Research & Development of Chinese Medicine (AKLPDCM202301) and China Postdoctoral Science Foundation (No. 2017M621789).

Data availability All data generated or analyzed during this study are included in the main texts and its supplementary information file.

Declarations

All experiments were performed in compliance with the relevant laws and institutional guidelines.

Conflict of interest The authors declare no competing interests.

References

1. Wei W, Zhou S, Ma DD, Li Q, Ran M, Li X, Wu XT, Zhu QL (2023) Ultrathin conductive bithiazole-based covalent organic framework nanosheets for highly efficient electrochemical Biosensing. Adv Funct Mater. https://doi.org/10.1002/adfm.202302917
2. Chen J, Lin K, Prasad S, Schmidtke DW (2023) Label free impedance based acetylcholinesterase enzymatic biosensors for the detection of acetylcholine, Biosens Bioelectron 115340. https://doi.org/10.1016/j.bios.2023.115340
3. Paneru S, Kumar D (2023) Ag-doped-CuO nanoparticles supported polyaniline (PANI) based novel electrochemical sensor for sensitive detection of paraoxon-ethyl in three real samples. Sens Actuat B: Chem 133270. https://doi.org/10.1021/acs.analchem.3c00099
4. Sidhu JS, Rajendran K, Mathew AB, Iqbal T, Saini DK, Das D (2023) Acetylcholine structure-based small activatable fluorogenic probe for specific detection of acetylcholinesterase. ANAL CHEM 19:7594–7602. https://doi.org/10.1021/acs.analchem.3c00099
5. Jiang Y, Miao Y, Ding Z, Lu Y (2023) In situ formed silicon-based nanoparticles enabled highly efficient dual-mode biosensing of chlorpyrifos. Food Chem 134243. https://doi.org/10.1016/j.foodchem.2022.134243
6. Li Y, Huang Z, Liu B, Huang Z, Yang H, Tan H (2023) Portable hydrogel test kit integrated dual-emission coordination polymer nanocomposite for on-site detection of organophosphate pesticides. Biosens Bioelectron 114890. https://doi.org/10.1016/j.bios.2022.114890
7. He C, Yan R, Gao X, Xue Q, Wang H (2023) Non-enzymatic electrochemical malathion sensor based on bimetallic Cu-Co metal-organic gels modified glassy carbon electrode. Sens Actuat B: Chem 133697. https://doi.org/10.1016/j.snb.2023.133697
8. Lopes DS, Miranda EV, Ando RA, Corio P (2023) SERS-based detection of an organochlorine pesticide through surface plasmon-induced C-C coupling, Environmental Science. NANO 7:1920–1931. https://doi.org/10.1039/d3en00123g
9. Yuan L, Gan Z, Fan Y, Ding F, Xu X, Chen X, Zou X, Zhang W (2022) Thermal-controlled active sensor module using enzyme-regulated UiO-66-NH2/MnO2 fluorescence probe for total organophosphorus pesticide determination. J Hazard Mater 129111. https://doi.org/10.1016/j.jhazmat.2022.129111

10. Shi Y, Zheng L, Liu R, Wu R, Zhang Z (2020) DNA-encoded MXene-Pt nanozyme for enhanced colorimetric sensing of mercury ions. Chem Eng J 136072. https://doi.org/10.1016/j.cej.2022.136072
11. Xu W, Fei J, Yang W, Zheng Y, Dai Y, Sakran M, Zhang J, Zhu W, Hong J, Zhou X (2022) A colorimetric/electrochemical dual-mode sensor based on Fe3O4@MoS2-Au NPs for high-sensitivity detection of hydrogen peroxide, Microchem J 107825. https://doi.org/10.1016/j.microc.2022.107825
12. Liu P, Zhao M, Zhu H, Zhang M, Li X, Wang M, Liu B, Pan J, Niu X (2022) Dual-mode fluorescence and colorimetric detection of pesticides realized by integrating stimulus-responsive luminescence with oxidase-mimetic activity into cerium-based coordination polymer nanoparticles. J Hazard Mater 127077. https://doi.org/10.1016/j.jhazmat.2021.127077
13. Xu W, Yang W, Dai Y, Fei J, Fan H, Zheng Y, Hong J, Liu J, Zhu W, Zhou X (2023) Dual-mode fluorescence and colorimetric determination of acetylcholinesterase accomplished by BSA-MnO2 QDs with oxidase-mimetic activity. Sens Actuat B: Chem 133503. https://doi.org/10.1016/j.snb.2023.133503
14. Zhao H, You Q, Zhu W, Li J, Deng H, Li MB, Zhao Y, Wu Z (2023) Nanoclusterzyme for dual colorimetric sensings: a case study on [Au14 (Dppp)5I4]2+. Small. https://doi.org/10.1002/smll.202207936
15. Zhao Y, Zhuang S, Liao L, Wang C, Xia N, Gan Z, Gu W, Li J, Deng H, Wu Z (2020) A dual purpose strategy to endow gold nanoclusters with both catalysis activity and water solubility. J AM CHEM SOC 2:973–977. https://doi.org/10.1021/jacs.9b11017
16. Chen S, Li Z, Huang Z, Jia Q (2021) Investigation of efficient synergistic and protective effects of chitosan on copper nanoclusters: Construction of highly active and stable nanozyme for colorimetric and fluorometric dual-signal biosensing. Sens Actuat B: Chem 129522. https://doi.org/10.1016/j.snb.2021.129522
17. Yang S, Peng L, Syzgantseva OA, Trukhina O, Kochetygov I, Justin A, Sun DT, Abedini H, Syzgantseva MA, Oveisi E, Lu G, Queen WL (2020) Preparation of highly porous metal-organic framework beads for metal extraction from liquid streams. J AM CHEM SOC 31:13415–13425. https://doi.org/10.1021/jacs.0c02371
18. Li H, Su C, Liu N, Lv T, Yang C, Lu Q, Sun C, Yan X (2022) Carbon dot-anchored cobalt oxyhydroxide composite-based hydrogel sensor for on-site monitoring of organophosphorus pesticides. ACS Appl Mater Inter 47:53340–53347. https://doi.org/10.1021/acsami.2c17450
19. Zhang B, Rong L, Zhou Z, Yuan W (2023) Ultra-stretchable, high-adhesive, self-healable and remoldable hydrogel sensor with dynamic multi-interactions for multiscale motion detection, Braille transmission and temperature monitoring. Chem EnG J 142305. https://doi.org/10.1016/j.cej.2023.142305
20. Jin R, Wang F, Li Q, Yan X, Liu M, Chen Y, Zhou W, Gao H, Sun P, Lu G (2021) Construction of multienzyme-hydrogel sensor with smartphone detector for on-site monitoring of organophosphorus pesticide. Sens Actuat B: Chem 128922. https://doi.org/10.1016/j.snb.2020.128922
21. Yan B, Cao Z, Hui C, Sun T, Xu L, Ramakrishna S, Yang M, Long Y, Zhang J (2023) MXene@Hydrogel composite nanofibers with the photo-stimulus response and optical monitoring functions for on-demand drug release. J Colloid Interf Sc I:963–971. https://doi.org/10.1016/j.jcis.2023.06.024
22. Zhong N, Gao R, Shen Y, Kou X, Wu J, Huang S, Chen G, Ouyang G (2022) Enzymes-encapsulated defective metal-organic framework hydrogel coupling with a smartphone for a portable glucose biosensor. Anal Chem 41:14385–14393. https://doi.org/10.1021/acs.analchem.2c03138
23. Ge D, Li M, Wei D, Zhu N, Wang Y, Li M, Zhang Z, Zhao H (2023) Enhanced activity of enzyme encapsulated in hydrophilic metal-organic framework for biosensing. Chem Eng J 144067. https://doi.org/10.1016/j.cej.2023.144067
24. Shen Y, Wei Y, Gao X, Nie C, Wang J, Wu Y (2023) Engineering an enzymatic cascade catalytic smartphone-based sensor for onsite visual ratiometric fluorescence-colorimetric dual-mode detection of methyl mercaptan. Environ Sci Technol 4:1680–1691. https://doi.org/10.1021/acs.est.2c07899
25. Tang K, Chen Y, Tang S, Wu X, Zhao P, Fu J, Lei H, Yang Z, Zhang Z (2023) A smartphone-assisted down/up-conversion dual-mode ratiometric fluorescence sensor for visual detection of mercury ions and l-penicillamine. Sci Total Environ 159073. https://doi.org/10.1016/j.scitotenv.2022.159073
26. Fu S, Chen H, Yang W, Xia X, Zhao S, Xu X, Ai P, Cai Q, Li X, Wang Y, Zhu J, Zhang B, Zheng JC (2022) ROS-targeted depression therapy via bsa-incubated ceria nanoclusters. Nano Lett 11:4519–4527. https://doi.org/10.1021/acs.nanolett.2c01334
27. Shen Y, Gao X, Chen H, Wei Y, Yang H, Gu Y (2023) Ultrathin C3N4 nanosheets-based oxidase-like 2D fluorescence nanozyme for dual-mode detection of organophosphorus pesticides. J Hazard Mater 131171. https://doi.org/10.1016/j.jhazmat.2023.131171
28. Liu Y, Wei X, Chen J, Yu Y, Wang J, Qiu H (2022) Acetylcholinesterase activity monitoring and natural anti-neurological disease drug screening via rational design of deep eutectic solvents and CeO2-Co(OH)2 nanosheets. Anal Chem 15:5970–5979. https://doi.org/10.1021/acs.analchem.2c00428
29. Yang W, Weng C, Li X, He H, Fei J, Xu W, Yan X, Zhu W, Zhang H, Zhou X (2021) A sensitive colorimetric sensor based on one-pot preparation of h-Fe3O4@ppy with high peroxidase-like activity for determination of glutathione and H2O2. Sens Actuat B: Chem 129844. https://doi.org/10.1016/j.snb.2021.129844
30. Li J, Gao M, Xia X, Cen Y, Wei F, Yang J, Wang L, Hu Q, Xu G (2023) Spherical hydrogel sensor based on PB@Fe-COF@Au nanoparticles with triplet peroxidase-like activity and multiple capture sites for effective detection of organophosphorus pesticides. Acs Appl Mater Inter 5:6473–6485. https://doi.org/10.1021/acsami.2c19921
31. Liu Y, Yang Z, Zhang X, He Y, Feng J, Li D (2019) Shape/crystal facet of ceria induced well-dispersed and stable au nanoparticles for the selective hydrogenation of phenylacetylene. Catal Lett 2:361–372. https://doi.org/10.1007/s10562-018-02648-9
32. Wang M, Choi S, Bai Q, Yu K, Guo W, Zhang F, Jia R, Qu F, Lin H (2023) Hollow Co-CeO2@PEG nanospheres: Ultrasound enhanced cascade-nanozyme for synergetic anticancer. Chem Eng J 140993. https://doi.org/10.1016/j.cej.2022.140993
33. Wang H, Yang W, Wang X, Huang L, Zhang Y, Yao S (2020) A CeO2@MnO2 core–shell hollow heterojunction as glucose oxidase-like photoenzyme for photoelectrochemical sensing of glucose. Sens Actuat B: Chem 127389. https://doi.org/10.1016/j.snb.2019.127389
34. Dong S, Dong Y, Liu B, Liu J, Liu S, Zhao Z, Li W, Tian B, Zhao R, He F, Gai S, Xie Y, Yang P, Zhao Y (2022) Guiding transition metal-doped hollow cerium tandem nanozymes with elaborately regulated multi-enzymatic activities for intensive chemodynamic therapy. Adv Mater 7:2107054. https://doi.org/10.1002/adma.202107054
35. Zhou T, Zhang T, Wang Y, Ge D, Chen X (2023) Polyoxometalate functionalizing CeO2 hollow nanospheres as enhanced oxidase mimics for ascorbic acid colorimetric sensing. Spectrochim Acta Part A: Mol Biomol Spectrosc 122219. https://doi.org/10.1016/j.saa.2022.122219
36. Yan Y, Hou Y, Zhang H, Gao W, Han R, Yu J, Xu L, Tang K (2021) CeO2 QDs anchored on MnO2 nanoflowers with multiple synergistic effects for amplified tumour therapy. Colloids Surfaces B: Biointerfaces 112103. https://doi.org/10.1016/j.colsurfb.2021.112103

37. Shahini MH, Mousavi M, Masoud Arabi A, Mahdavian M, Ramezanzadeh B (2021) Ce-oxide quantum dots decorated graphene oxide (CeO-QDs-GO) nano-platforms synthesis and application in epoxy matrix for efficient anti-corrosion ability. J Ind Eng Chem 51–65. https://doi.org/10.1016/j.colsurfb.2021.112103
38. Dai Y, Xu W, Hong J, Zheng Y, Fan H, Zhang J, Fei J, Zhu W, Hong J (2023) A molecularly imprinted ratiometric fluorescence sensor based on blue/red carbon quantum dots for the visual determination of thiamethoxam. Biosens Bioelectron 115559. https://doi.org/10.1016/j.bios.2023.115559